Epitaxy Orientation and Kinetics Diagnosis for Zinc Electrodeposition

Jin Zhao[1], Zehua Chen[2], Zhihui Chen[1], Zeyi Meng[1], Jianwei Zhang[3], Wenjie Lv[1], Congshan Guo[1], Zhizhen Lv[1], Shouce Huang[1], Yang Yang[2], Zhongfan Liu[1,4,5]*, Jingshu Hui[1]**

[1]College of Energy, Soochow Institute for Energy and Materials InnovationS (SIEMIS), Key Laboratory of Advanced Carbon Materials and Wearable Energy Technologies of Jiangsu Province, Jiangsu Key Laboratory of Advanced Negative Carbon Technologies, Soochow University, Suzhou, 215123, P. R. China

[2]Theoretical Chemistry Institute and Department of Chemistry, University of Wisconsin-Madison, Madison, Wisconsin, 53706, United States

[3]Institute of Functional Nano and Soft Materials (FUNSOM), Jiangsu Key Laboratory for Carbon-Based Functional Materials and Devices, Soochow University, Suzhou, 215123, P. R. China

[4]Center for Nanochemistry, Beijing Science and Engineering Center for Nanocarbons, Beijing National Laboratory for Molecular Sciences, College of Chemistry and Molecular Engineering, Peking University, Beijing, 100871, P. R. China

[5]Technology Innovation Center of Graphene Metrology and Standardization for State Market Regulation, Beijing Graphene Institute, Beijing, 100095, P. R. China

E-mail: yyang222@wisc.edu (Y. Yang); zfliu@pku.edu.cn (Z. F. Liu), jshui@suda.edu.cn (J. S. Hui)

ABSTRACT. Accurate assessment of the electrodeposition mechanism is essential for evaluating the electrochemical stability and reversibility of metal anodes. Multiple strategies aimed at uniform Zn deposition have been extensively reported, yet it is challenging to clarify the Zn crystal growth regularity and activity due to the obscured physicochemical properties of as-deposited Zn. Herein, we present a protocol for elucidating the controlled epitaxial growth process of Zn crystal and quantifying their surface electrochemical activity using scanning electrochemical microscopy. We find that the early-stage epitaxy tends to form stacked-multilayer structure accompany with intermittent rotation. The site-dependent kinetics and morphology correlation reveal distinct evolution path at early and final stages. Our exploration advances the understanding of Zn growth mechanism and paves the way for realization of the interface kinetics of metal batteries in situ.

KEYWORDS: Zn deposition, epitaxy orientation, (002) crystal planes, morphology and kinetics evolution, scanning electrochemical microscopy

Electrodeposition is a method that forms plating layers through the migration of anionic and cationic ions in the electrolyte under the influence of an external electric field and the redox reaction on the electrode surface.[1, 2] The reversibility of electrochemical deposition/stripping process is one of the key factors that influence the energy storage property of metal anode-based batteries.[3-5] Nevertheless, this reversibility is severely harmed by the dendritic electrodeposition of metals, which usually combines with other side reactions such as corrosion, passivation, and gas evolution and results in premature failure and short-circuiting of high-capacity metallic battery anodes.[6-9] Recently, the deposition behaviors of various metal anodes have been reported, illustrating their tendency to form loose and irregular branching,[10] spheroid,[11] fibrous,[12] and sheet structures,[13] etc. To overcome this unfavorable tendency, regulating the facial orientation distribution of deposited crystals has been reported as effective strategies to regulate the electrodeposition behavior. One such effort is to construct low-lattice mismatch conductive interface layers of the target anode.[3, 14]

Among various metal anode systems, Zinc (Zn) stands out due to its relatively high capacity (820 mA h g^{-1}, 5855 mA h cm^{-3}), inherent security, and cost benefits.[15-17] As a hexagonal close-packed (HCP) metal, Zn typically exhibits the (002), (100), and (101) crystal planes as its dominant crystallographic features.[13, 18, 19] The morphology of Zn deposition can be influenced by several factors: (i) Intrinsic properties of the substrate electrode affect the crystalline structure of the initial

nucleation;[20-22] (ii) Faradaic reaction, interfacial kinetics and the ion concentration at the electrode surface determine the Zn electrodeposition process;[23, 24] (iii) Zn^{2+} diffusion near anode-electrolyte interface contribute to the final deposition morphology.[25, 26] Many studies have been performed to regulate the Zn deposition morphology and induce the (002) crystal structure by modifying the substrate electrode,[27, 28] altering the electrolyte solvation structure,[29, 30] and synthesizing an artificial electrode-electrolyte interphase layer.[31, 32] However, the majority of them focused on employing these controlling factors to achieve great final deposition architecture and battery cycling performance, yet how these factors affect the deposition process, especially at the initial stage, is rarely addressed.

To further investigate the in-depth factors that influence the electrodeposition mechanism, it is crucial to consider the functional association with preferred Zn deposition orientation, the deposition potential, and the surface energy between the deposit and the substrate electrode.[10, 33, 34] The deposition structure with the optimal (002) direction exhibits a smooth equipotential plane and the lowest surface energy, making it electrochemically less active.[35, 36] Compared with the other crystallographic planes, the epitaxial growth of the (002) crystal structure plays a critical role in maintaining the high reversibility and high Faradic efficiency of Zn anodes.[3, 37] Nevertheless, the random orientation between different deposition domains can result in additional issues during battery electroplating, including the formation of uneven Zn deposits and eventually the loose and porous dendritic structure.[38-40] In addition, the interfacial kinetics influence on the Zn deposition also play an important role, which the electrodeposition must be implemented within the kinetic limitation.[24, 41] Modulating Zn crystal orientation and alignment could effectively regulate the dendrite growth, as the substrate plays a significant role in controlling Zn deposition morphology at the initial stage.[40] However, after exceeding a critical thickness, more complex deposition protocols could prevail over the initial homoepitaxy and dominate the growth texture.[10, 40, 42, 43] Unfortunately, there has been little discussion and insight into this aspect.

In this work, we comprehensively examine the morphology and kinetic evolution mechanism of the full-cycle Zn electrodeposition process at the microscopic level. A distinct electrodeposition phenomenon is observed on a low lattice-mismatch highly oriented pyrolytic graphite (HOPG) substrate. We observe the transition from the formation of 2D horizontally expanded multilayer Zn crystal domain to 3D bulk Zn crystal. Additionally, irregular growth patterns of 2D Zn sheets,

such as dislocation center and single domain rotation, are identified. Using scanning electrochemical microscopy (SECM), the kinetic evolution mechanism of individual Zn domains is quantified during the deposition process, with oriental crystal edges and centers exhibiting distinct activities that influence future deposition. The highly active bulk Zn crystals formed after long-term deposition are also explored. Our spatially resolved study of Zn electrodeposition kinetics highlights the importance of (002) crystal plane extension in Zn deposition and provides valuable insights into kinetic quantification into the electrodeposition mechanism across a wide spectrum of metal anodes.

Hexagonal texture evolution behavior of Zn deposition process. To visualize the incubation and evolution of Zn deposition mechanism, large and homogeneous Zn crystals are preferred for comprehensive analysis. To enable a horizontal Zn platelet deposition, the commercial HOPG with a low lattice-mismatch interface was selected as the deposition substrate (**Figure** S1). We got a maximum average Zn crystal diameter of 25 μm at fine-controlled conditions of electrolyte concentrations (**Figure** S2) and current densities (**Figure** S3). With this understanding, we have observed the whole morphological evolution process of Zn electrodeposition, from Zn nucleation, planar growth, to bulk Zn crystal cumulation. As shown in Figure 1a–1c, three different Zn crystal growth phenomenon were observed: spiral growth, stacking and extrusion. Instead of homogeneous expansion to form the traditional hexagonal Zn sheet, the Zn grows spirally around the seed while enlarged, which will continue to stack on top of the base plane to form multipalyer structure, and some case of interlaminar extrusion can be found as well, as shown in Figure 1a. While the upper-layer homoepitaxy tends to maintain similar symmetry as the bottom layers, the Zn crystal enventually form a multilayer stacking structure (Figure 1b and S4). Due to the spiral type growth mechanism, there is a large chance to find screw dislocation close to nucleation center (Figure 1a, 1b). Furthermore, two nearby Zn crystal expansion leads to an extrusion at boundaries (Figure 1c). These defects are the potential origins for uncontrolled vertical growth to form dendrites. Figure 1d schematically demonstrates the entire bulk Zn crystal growth process: from 0D Zn nucleation (Stage–1), 2D hexagonal Zn crystal horizontal expansion (Stage–2), horizontal and vertical mixed alignments of Zn flakes (Stage–3), to 3D bulk growth (Stage–4) on the HOPG surface.

At the beginning of Zn electrodeposition, Zn^{2+} diffusion provided the resource for Zn electrodeposition, which conducted 0D Zn nucleation on HOPG as shown in Figure 1d (Stage–1) and Figure 1e. After that, the formation of isolated hexagonal Zn sheets was observed under deposition capacity of 0.16 mA h cm^{-2} (Stage–2), with preferential expansion along the (002) plane (Figure 1b). Our finding of this dominated growth along the (002) plane agrees well with current researches, where the of Zn atom on (100) plane is thermodynamically favored over that on the (002) plane.[36, 44] Typically, the epitaxy is not a homogeneously distributed single crystal (will be discussed in the next section), they tend to form multilayer-stacked structures combined with different degrees of rotation among domains (Figure 1f). This interaction between HOPG and Zn (i.e. binding energy) is sufficient to generate these stacking and rotation.[45, 46] With accumulated Zn deposition reaching 0.8 mA h cm^{-2}, these isolated horizontal Zn domains will cover the entire substrate surface and start to form uncontrolled vertical-horizontal orientations mixed deposition (Stage–3, Figure 1g), and eventually buildup 3D bulk features (Stage–4, Figure 1h) when the deposition capacity reaches to 5 mA h cm^{-2}. In the latter two stages, the vertically grown Zn deposits are typically regarded as the origin of hazardous dendrite growth. This deposition Stage transition agrees with the calculated Sand's time of 645 s (see supporting information for more detail). The detailed full-spectrum morphological evolution with increasing deposition capacity is shown in Figure S5. Moreover, in this semi-coherent epitaxy growth, the substrate lattice plays a key role in controlling the Zn deposition texture at the initial growth stage. Electron backscatter diffraction (EBSD) inverse pole mapping and X-ray diffraction (XRD) pattern of HOPG substrate demonstrates an exclusive (002) crystalline plane dominant structure (Figure S6–S7), which agrees verified characteristic graphite behavior with I (2D)/I (G) < 1 (Figure S8)[47, 48]. When the plating starts, the Zn^{2+} in solution will diffuse to electrode surface, transfer electrons, and form epitaxial structure on HOPG surface. Benefiting from the low lattice mismatch of HOPG and Zn, the reduced Zn atoms regularly arranged to form hexagonal-type Zn flakes (Stage–2). However, this crystal expansion at Stage–2 is not always an isotropic process, as evidenced by the early-stage morphologies of different domains (Figure S9). Therefore, the Zn growth front expansion and rotation rates play important roles in determining the size of Zn domains. Moreover, not only thermodynamic controls the epitaxial deposition, but also the kinetic parameters such as current density, potential bias and electrolyte contribute to this process.

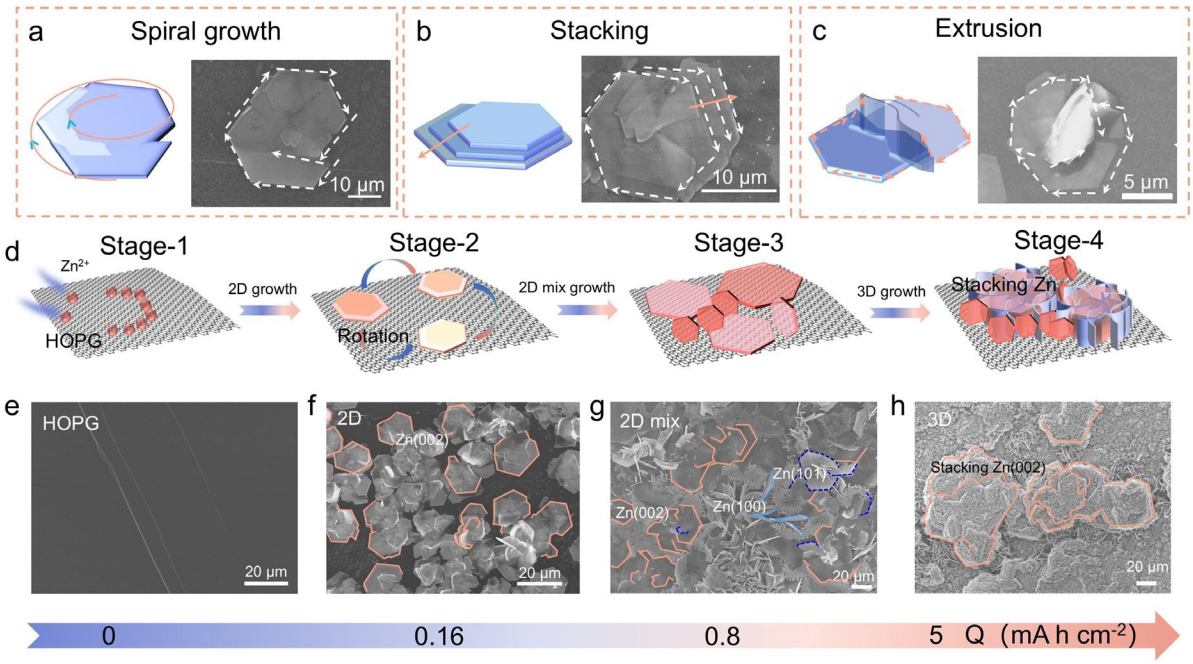

Figure 1. Zn epitaxial deposition processes. (a-c) Three different Zn crystal growth mode with (a) Epitaxial spiral growth, (b) Extended stacking, and (c) extrusion, each panel has a diagram and example SEM image. (d) Diagrams of different stages of Zn deposition on HOPG. (e-h) SEM images of different Zn deposition stages, with areal deposition capacity of (e) 0, (f) 0.16, (g) 0.8, and (h) 5 mA h cm^{-2}. Deposition condition: 1 M $ZnSO_4$ electrolyte, 5 mA cm^{-2} current density.

Characteristics of single domain Zn deposits with (002) dominant facets. The Zn deposition morphology on the HOPG surface corresponds to the HCP structure of metallic zinc, as shown in the lattice structure in Figure 2a.[1, 40] SEM images in Figure S4 showed the morphology of the Zn crystal layer stacking, and extended (002) plane simultaneously. In this context, the crystal orientations of deposited Zn were characterized by XRD in Figure 2b, with (002) crystal plane as the dominant orientation. Atomic force microscope (AFM) was applied to measure the surface structure and height changes between 2D layers. The height and width details of the Zn domain was demonstrated by topographical mapping (Figure 2c) and line scan profile (Figure 2d). The lamellar stacking of hexagonal Zn sheet demonstrated a variation of step height from ~10 nm to ~50 nm.

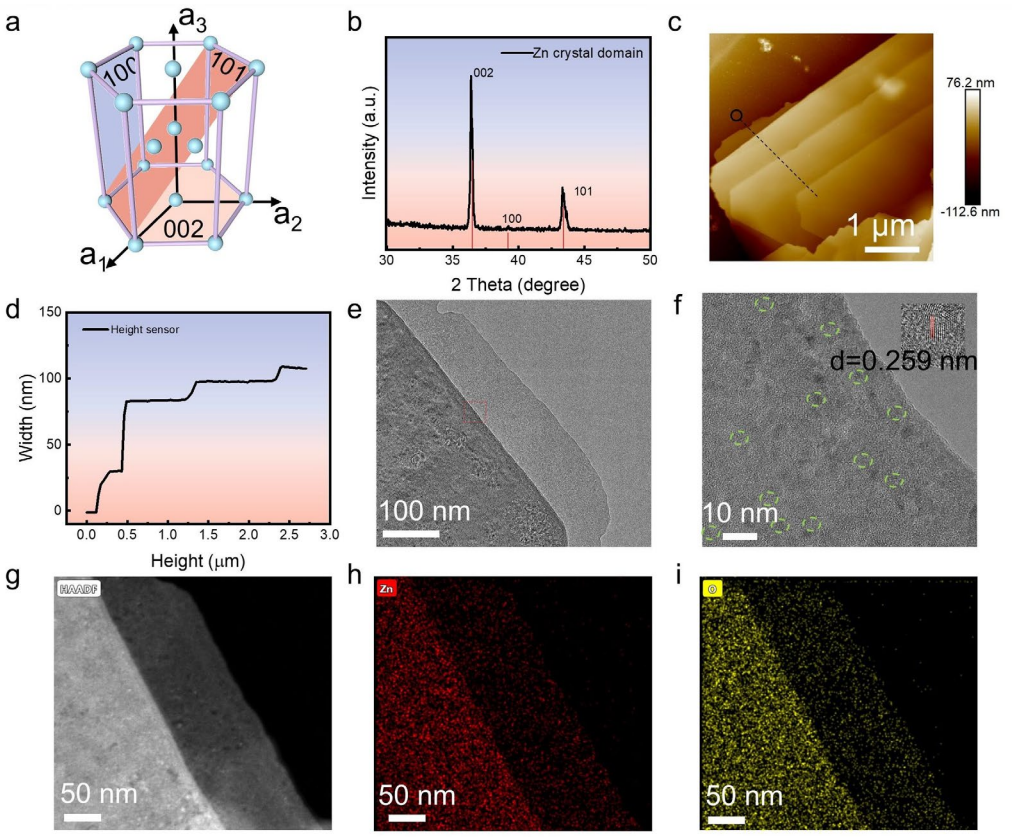

Figure 2. (a) Schematic diagram of the HCP structure of Zn with (002), (100) and (101) crystal plane. (b) XRD patterns for Zn deposition on the HOPG surface at early stage. (c) AFM images of the edge section of bilayer Zn domain. (d) Line scan height difference of selected section in panel c. (e) HRTEM image of the deposited Zn platelet. (f) Zoom-in HRTEM image of Zn platelet edge with labeled (002) domains. (g) HRTEM images and the corresponding EDS mappings of (h) Zn and (i) O element. The sample for HRTEM and EDS-mapping measurements was prepared by plating Zn on HOPG at 0.16 mA h cm^{-2} capacity.

High-resolution transmission electron microscopy (HRTEM) images and energy-dispersive X-ray spectroscopic (EDS) mapping results were employed to probe the surface structure, component, and crystalline orientation of deposited Zn. As illustrated in Figure 2e, the HRTEM image displayed the edge section of bilayer-stacked Zn deposit. To analyze the surface and lattice structure information of deposited Zn crystal, we observed a polycrystalline structure with obvious interplanar spacings of 0.259 nm in Figure 2f, corresponding to Zn (002) plane. Furthermore, homogeneous distributions of Zn and O were observed in this region (Figure 2g-i). To avoid the

uncertainty of the measurement, we also measure the surface morphology and lattice information of the whole crystal domain in Figure S10. In summary, the lamellar stacking of Zn crystals occurred during the growth process, which is also accompanied by the appearance of heterogeneous lattice orientation.

Intermittent rotation of epitaxial Zn crystals. Apart from the extension and stacking structure within each Zn domain at Stage–2, an intermittent variation in rotation angle was observed among different epitaxial domains on the semi-coherent Zn/HOPG interface.[49, 50] For statistics on these angle variations, we manually designated one edge of a single crystal as the inner reference (0° rotation) and measured the rotation angle of other domains relative to it (Figure 3a). Because of the C_6 rotational symmetry of deposited Zn, the in-plane ordered rotation of Zn crystals is expected to repeat every 60°, as shown in Figure S11. Note that although this angle distribution is measured against a chosen Zn edge, fundamentally, it is essentially the same as the angle

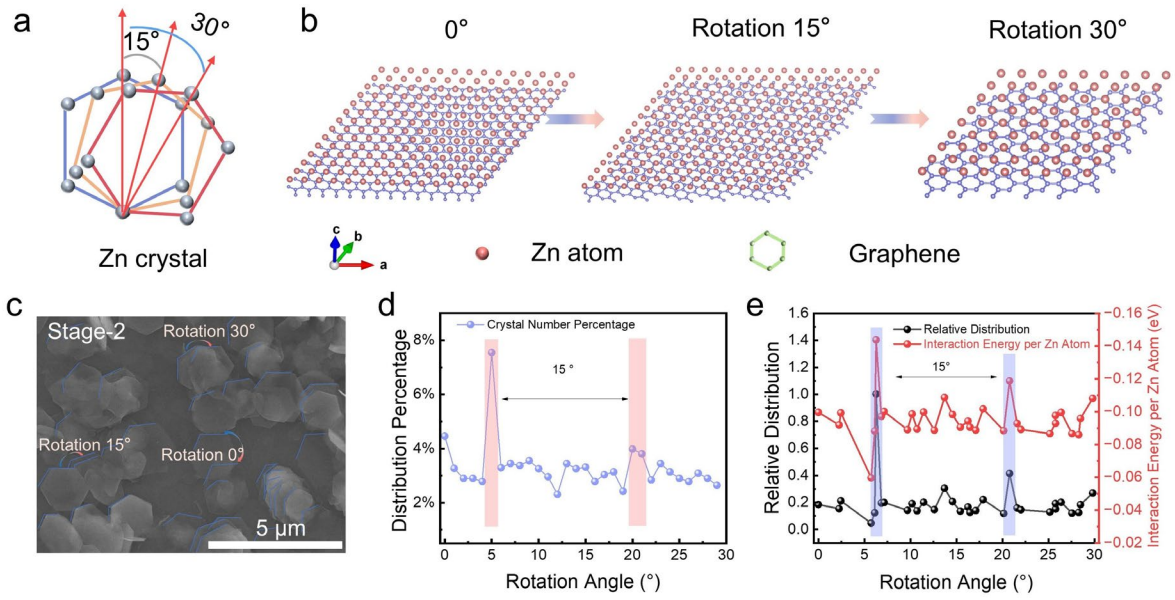

Figure 3. (a) Schematic of Zn crystals with different in-plane rotation degrees, marked with 15° and 30°. (b) Atomic structure of the Moiré superlattice pattern between Zn and graphene with a twist angle of 0°, 15° and 30°. (c) SEM images of Zn deposition crystals on HOPG at Stage–2. (d) The statistic Zn crystals rotation distribution at Stage–2, which is obtained based on SEM images multiple samples at 0.16 mA h cm^{-2} deposition capacity. (e) Calculated interaction energy per Zn at different rotation angles between Zn and graphene lattice using PBE-D3(BJ) and simulated relative rotation angle distributions using a Boltzmann distribution at 300K.

distribution relative to the HOPG substrate, whose topmost layer is graphene. The honeycomb structure of the graphene induces a homoepitaxial deposition of Zn. Since graphene and Zn have different lattice constants, different Moiré patterns occur as a function of the relative rotation angle. Figure 3b exhibited the Moiré with different rotation angles (0°, 15° and 30°) between Zn and the HOPG lattice. SEM images in Figure 3c clearly demonstrated the deposition topography and the relative rotation angles at Stage–2. Figure 3d summarizes the experimentally observed rotation angle distribution curves at Stage–2, which was obtained through statistical analysis of SEM images with *c.a.* 2000 epitaxial Zn domains over the HOPG substrate (Figure S12 and Table S1). We found that the rotation angle distribution of crystals peaks at around 5° and 20°.

To rationalize the experimental findings, we calculated the interaction energies using a Zn and graphene bilayer model as a function of different rotation angles at their optimal inter-layer distances (Figure 3e and S13, See Methods for details). This bilayer model can provide insights into the initial Zn deposition process on the HOPG surface. We observed that the interaction energy per Zn atom varies slightly with different rotation angles, which reaches its local maximal values of -0.14 eV and -0.12 eV at 5° and 20°, respectively. Based on these interaction energies, we predicted the relative population using a Boltzmann distribution at 300K, and the result is also shown in Figure 3e. Intriguingly, this predicted distribution is in great agreement with the experimental crystal angle distribution in Figure 3d. Therefore, we conclude that because of an energetic preference, the low-mismatch HOPG lattice can align the otherwise randomly distributed Zn crystal with an angular separation close to 15°. As a result of these angular differences and domain expansions, the crystals exhibit a 2D mixed Stage–3 during the deposition process, which is consistent with the SEM images in Stage–3 (Figures 1g).

Heterogeneous electrochemical kinetics of single Zn domain. To better present the relationship between morphological evolution and kinetics evolution mechanism during Zn electrodeposition process, we use scanning electrochemical microscopy (SECM) to identify topographical characteristics and the relevant kinetics variations in situ. The electroplating of Zn on HOPG substrate is a hybrid process. While the property of HOPG substrate only determines the original heteroepitaxy Zn formation (Zn on HOPG), the property of the initially formed Zn layer controls the following homoepitaxy process (Zn on Zn). Therefore, the electrochemical activity of different crystal planes plays an important role in controlling the Zn deposition

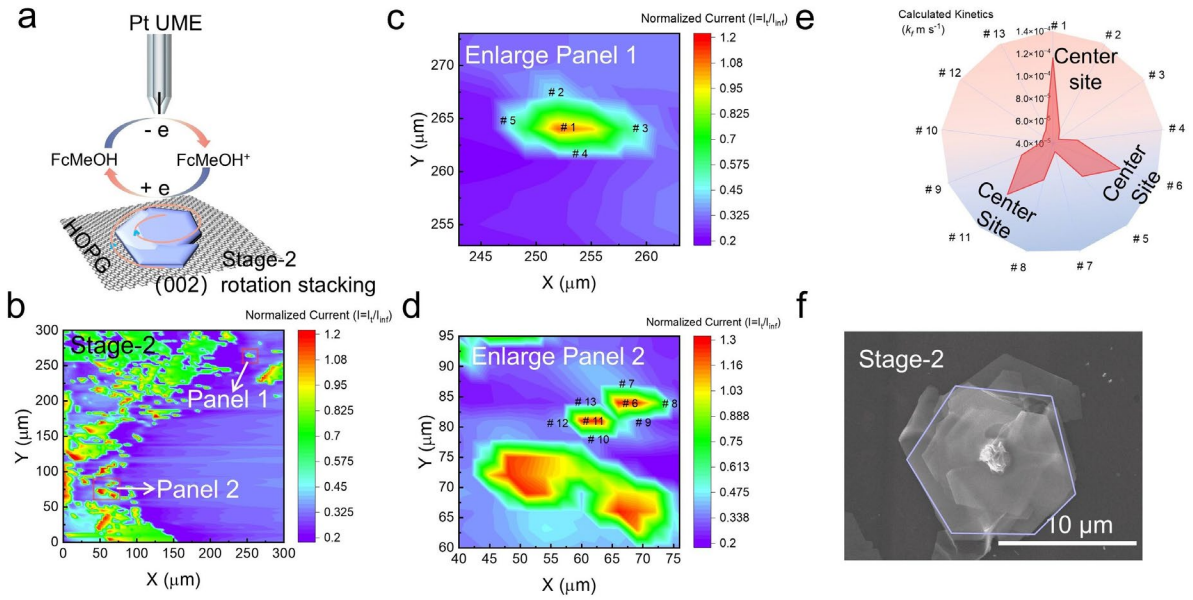

Figure 4. Heterogeneous activity distribution of as-grown Zn domains. (a) Schematic diagram of SECM feedback image. (b, c, d) SECM image and corresponding enlarge area of Stage–2 Zn deposition sample with marked active sites. (e) The calculated k_f values of different sites labeled in panel c and d. (f) The similar SEM image of spiral epitaxy growth orientation.

mechanism. The conventional approach is limited to the computational calculation, which models the binding energies of Zn atoms on various crystal planes under ideal conditions.[14, 51] Noteworthy, SECM has been demonstrated as a powerful technique for mapping surface electron transfer reactivity and morphology with high spatial and temporal resolution, providing complementary local electrochemical information apart from morphology information from SEM and TEM observations.[52] As shown in Figure 4a, feedback from the substrate is reflected by the redox current fluctuation of the redox mediator ferrocene-methanol (FcMeOH) oxidation, when the tip approaches the substrate surface. The SECM images of Stage–2 as-deposited Zn are shown in Figure 4b. The SECM image clearly illustrates the different charge transfer activity between the HOPG surface (blue region) and individually distributed as-deposited Zn domains (green and red region), which obtained a distinct contrast with blank HOPG (Figure S14). The corresponding optical microscope (OM) of the same examined area is shown in Figure S15. If we take a closer look at these Zn domains (Figures 4c and 4d), the hexagonal patterns of the Zn epitaxy become recognizable. Interestingly, the center and edge of each Zn crystal displayed divergent tip currents with positive feedback (red-yellow region, $I_t/I_{inf} > 1$) and negative feedback (green region, $I_t/I_{inf} < 1$), respectively. These heterogeneities on SECM mappings yield distinct crystal growth kinetics

between center and edge regions, which means that under the influence of electrical field and electrolyte modulation, the center of the as-grown Zn domain has a higher electron transfer activity compared to the edge. The center dislocation originate from spiral growth may be the main reason for this enhance local kinetics.

Trying to verify the relative kinetics difference of (002)–dominant center and (100)–dominant edge sites, approach curves were carried out to quantify the heterogeneous charge transfer rate constants (k_f) of several selected sites of Zn domains (labelled in Figure 4c, d). As shown in Figure S16 and S17, the approach curves show a dramatic activity change between center and edge sites, with mathematically fitted k_f showing the order of magnitude difference (approximately 1.2×10^{-4} m s^{-1} for center sites and 5×10^{-5} m s^{-1} for edge sites) (Figure 4e). Apart from the crystal plane-originated activity differences, the local dislocation protuberance may have an additional contribution to the enhanced activity of center sites. Fortunately, we observed the topography of spiral epitaxy growth with a prominent central site, which is consistent with the electrochemical analysis by SECM (Figure 4f). Additionally, the optical microscope image of as-grown Zn also revealed smooth and uniform morphological features on edge sites and subtle longitudinal prominent features on the center sites (Figure S18). However, the higher center activity of as-grown Zn results in faster surface passivation once contacting with electrolyte[53], as evidenced by the high-resolution SECM image using a 500 nm radius tip (Figure S19). Convincingly, the kinetics properties of Zn domain deposited on HOPG show recognizable heterogeneity between center and edge regions, consistent with the results mentioned in Figure 1.

Kinetics evolution mechanisms of Zn deposits at final stage. In addition to studying the epitaxial growth mechanism at early stage (Stage–2 and Stage–3), we also reveal why the growth orientation cannot be controlled merely by the substrate. SECM was used to quantify the dynamic evolution during the Zn deposition process from capacity of 0.16 mA h cm^{-2} to 0.25 mA h cm^{-2} (Figure S20), where we found the newly formed Zn deposits present positive feedback. Given the transient positive to negative feedback transition along the bottom-up SECM scanning direction (Figure S20b), the passivation process of newly formed Zn crystal was so fast that the top-part of scanned area turned to less active response before SECM tip arrived. When the areal capacity increased to 0.8 mA h cm^{-2}, the horizontal (002) and vertical (101 and 100) mixed sample was observed by XRD and SECM (Figure S21 and S22). The related SEM images are shown in Figure

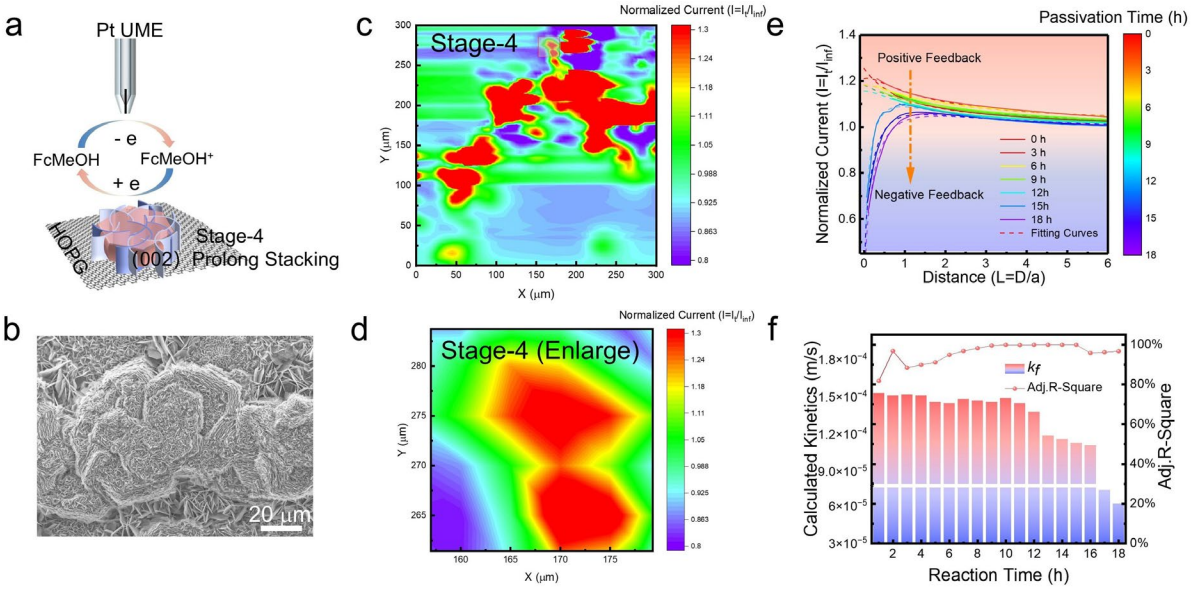

Figure 5. (a) Schematic illustration of SECM feedback mode with mediator FcMeOH on bulk Zn crystals after long-time deposition. (b) The corresponding SEM images of bulk Zn crystals after Stage 4 deposition. (c) SECM feedback images and (d) the corresponding enlarged aera of electrodeposition behavior. (e) The approach curves transition time of electroactive from positive feedback to negative feedback for newly grown dendrite to passivate dendrite. (f) The calculated k_f values comparison and fitting error with different reaction time.

S23, consistent with the morphology of Stage–3. As the electrodeposition capacity increased to 5 mA h cm^{-2} (Stage–4) in Figure S24, the bulk crystal structure formed an obvious hexagonal pattern composed of (101) topography (Figure 5b and S25), consisting of multiple fastigiate–type horizontal crystals and vertical dendrites. Figure 5c and 5d illustrated the SECM images of Stage–4 Zn deposits and the corresponding zoomed-in area. The similar hexagonal pattern between localized positive feedback and SEM morphologies confirms the homogeneous high activity on entire Stage–4 Zn epitaxy. Intriguingly, the surface of this bulk crystal illustrated strong resistance towards solution passivation compared to early stages, it took up to 18 h to finish the entire transition in Figure 5e and 5f. Suggesting that the kinetics passivation of stacking crystals is transformed progressively. Hence, investigation of localized reactivity on anode interface effectively elucidates the Zn deposition kinetics transformation process, which plays an essential role for the surface-level evolution in deposition morphology, and further impacted the service life of the battery in the overall cycling process. Comprehensively, this is of great significance to understand the key scientific relationship between the electrochemical deposition morphology and kinetics behavior and the cell to stably operating of the other metal ion battery.

Influence of graphitic substrate on cycling performance of Zn electrodeposition. To assess the potential commercialization for high energy batteries, the Zn/graphite half-cells have been further investigated. The plating/stripping tests of graphite paper and carbon paper were carried out in coin cells with 5 mA cm^{-2} and 1 mAh cm^{-2}. Benefiting from a low lattice-mismatch interface between Zn and graphite, the Zn|Graphite asymmetric cell exhibits superior stability closed to 1000 h, while the Zn|Carbon half-cell suffer from short circuit after 400 h of cycling, as shown in Figure 6a. The Zn|Graphite asymmetric cell maintained a high level corresponding coulombic efficiency (CE) of average 99.49% (Figure 6b). Furthermore, control the capacity at Stage–2 give the most stable cycling performance with rapid stabilization and lower overpotential compared to other stages, confirmed the best reversibility of horizontally packed Zn plates (Figure 6c). Furthermore, as shown in the capacity vs. voltage curves at the 10th, 50th and 100th cycles, the Zn|Graphite cell maintains lower overpotentials, along with high coulombic efficiency (Figure 6d). Figure 6e exhibits the charge and discharge curves of Zn|Graphite cell at various capacities from 0.16 mAh cm^{-2} to 5 mAh cm^{-2} with lower overpotentials (16.5 mV, 17.9 mV and 18.8 mV). The corresponding comparison of overpotentials and CEs between Zn|Graphite and Zn|Carbon cells are shown in Figure 6f and S26. Compared to the graphite paper, the carbon paper is lacking of well-organized graphitic lattice modulation, the Zn|Carbon shows a higher overpotentials and lower CEs in comparison to Zn|Graphite cells. XRD patterns and SEM images were taken to demonstrate Zn deposition characteristics after 10 cycles in Figure 6g, 6h and S27, which evidenced a homogeneous Zn (002) crystalline plane dominant structure and the continuous extension from the graphite substrate. The electrochemical characterization of Zn|Graphite asymmetric cells before and after cycling are well-aligned with the Zn deposition mechanism on the HOPG surface described above. Consequently, the Zn|Graphite cell exhibits enhanced stability and promoted cycling performance, substantiating its prospective commercial application.

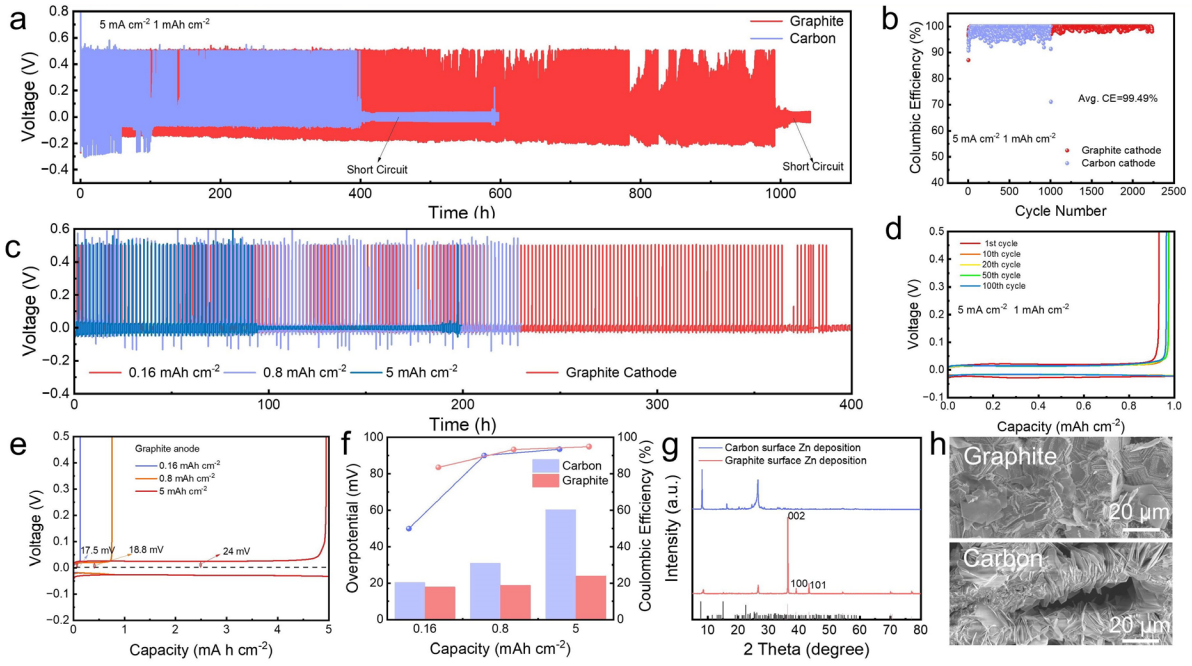

Figure 6. Electrochemical performance of Zn deposition on different carbon-based substrates. (a) Cycling performance of the Zn|Graphite and Zn|Carbon half-cells under an areal capacity of 1 mAh cm^{-2} and a current density of 5 mA cm^{-2}, where the asymmetric cells were set to a cut-off voltage of 0.5 V vs. Zn/Zn^{2+}. (b) Coulombic efficiencies (CE) of Zn|Graphite and Zn|Carbon asymmetry batteries at 5 mA cm^{-2}, 1 mAh cm^{-2}. (c) Cycling performance of Zn|Graphite half-cells with operating 1 h at various areal capacities of 0.16 mAh cm^{-2}, 0.8 mAh cm^{-2}, 5 mAh cm^{-2}, corresponding to Stage–2, Stage–3 and Stage–4 conditions, respectively. (d) Capacity vs. voltage curves at different cycles. (e) Charge and discharge curves of the Zn|Graphite half-cells with different stage capacities and a cut-off voltage of 0.5 V vs Zn/Zn^{2+}. (f) The corresponding overpotentials and CEs of graphite and carbon paper substrate. (g) XRD patterns and (h) SEM images of the Zn electrodeposition on graphite paper and carbon paper after 10 cycles with an areal capacity of 1 mAh cm^{-2} and a current density of 5 mA cm^{-2}.

In summary, we demonstrated that morphology and kinetics evolution mechanism during Zn crystals deposited on HOPG substrate. Using multiscale characterization analysis (SEM, AFM, HRTEM, OM and SECM), direct visualization of Zn domain nucleation and growth process were achieved (Stage–1 to Stage–4), especially those of out-plane (002) epitaxial stacking and in-plane rotation at early stage were extensively discussed. The growth tendency during deposition calendar is to extend the (002) crystal planes with horizontal and vertical mixed structures, while the substrate plays a key role in controlling the texture at the initial growth stage, and its influence gradually decays as deposition proceeding. We quantified the correlated Zn domain electron transfer activity and consequent morphology evolution via SECM. Site-dependent kinetics variation at Stage–2 single Zn sheet was studied, with center site of hexagonal domain exhibiting

higher activity and an increased tendency for future deposition and passivation. As a comparison, the Stage–4 bulk Zn crystals demonstrated strong resistance towards passivation. Furthermore, we also conduct Zn|Graphite as asymmetric cells to evaluate the nucleation process, Zn plating/stripping behavior and CE, in agreement with the Zn deposition mechanism on the HOPG surface. Our finding of distinct mechanisms at different growth stages could help unravel the mystery of evolved charge-discharge curves in Zn-ion battery field. This work provides an approach to elaborate morphology and kinetics behavior of Zn epitaxy, which paves the way towards metal deposition kinetics of other advanced metal anode-based energy storage systems in the near future.

METHODS

Materials

The $ZnSO_4 \cdot 7H_2O$ salt (purity ≥99 %), Ferrocenemethanol (FcMeOH, ≥97%), and ultrapure water (HPLC level) were purchased from Aladdin and used directly without further treatment. Highly Oriented Pyrolytic Graphite (HOPG) and graphite paper were purchased by Jiangsu XFNANO Materials Technology Co. LTD. The glass fiber (GF) of Whatman was purchased from Cytiva Co. LTD. 10 μm Pt wire (≥99.99%) was purchased from Zhongnuo Advanced Materials Technology Co. LTD. Zn foil (≥99.99%) was purchased from Xinji Metal Materials Co. LTD.

Characterizations

The morphologies of Zn deposits were characterized by an optical microscope (OLYMPUSBX 53) and SEM (Hitachi SU 8010). SEM images were obtained at 10 kV acceleration voltage and 10 μA emission current. High-resolution transmission electron microscope (HRTEM) images and energy dispersive X-ray spectroscopy (EDX) are acquired by the Talos F200X transmission electron microscope. The deposited Zn flakes was scraped with a scalpel, dispersed in an ethanol solution under ultrasonication and transferred to carbon-based Cu mesh. X-ray diffraction (XRD) spectra were measured by Bruker D8 Advance with Cu-Kα ray radiation (λ = 1.5406 Å), using an operating voltage of 40 kV and 40 mA current. Atomic force microscope (AFM) is performed in the tapping mode by Bruker Dimension Icon. Raman spectra were collected in 532 nm laser wavelength from HORIBA Evolution.

Electrochemical measurements

All electrochemical experiments were collected using a CHI 920D SECM from CH Instruments in a four-electrode setup under the condition of atmosphere, as previously described.[53] A homemade Teflon cell contained a four-electrode arrangement with a Zn wire counter electrode and a commercial Ag/AgCl reference electrode (CH Instruments) in all cases. All experiments were conducted in a Faraday cage at room temperature. Chronopotentiometry (CP) experiments of the Zn symmetrical system were tested in 0.5–1M $ZnSO_4$ aqueous electrolyte with a current density of 0.1–5 mA cm^{-2}. The linear scan voltammetry (LSV) curves were performed through three-electrode configurations with HOPG as the working electrode, Zn as the counter electrode, and Ag/AgCl as a reference on an electrochemical workstation between 0 to -1.2 V at a scan rate of 10 mV/s. The Tafel curves were carried out on a three-electrode system in which Zn deposits were formed on HOPG as a working electrode. The potential range was set between -0.6 to -1.2 V (vs. Ag/AgCl) at a scan rate of 10 mV s^{-1}.

SECM Feedback Images measured the bulk and localized kinetics information of various conditions of Zn domain structures. The HOPG with deposited Zn was used as substrate electrode, a Pt UME with the radius of 5 μm and 500 nm were used as working electrode in different experiments. All experiments were performed in 1 M $ZnSO_4$ aqueous solution with 1 mM FcMeOH as the mediator. In terms of feedback SECM imaging, the process involves the imaging of an ultramicroelectrode scanning at a constant height above the surface of HOPG substrate (+z direction constant height of 10 μm). The Faraday current on the probe surface is observed to change in accordance with the undulations and electron transfer activity of the substrate. The approach curve is an SECM technique to measure the chemical reactivity of an interface on micro and submicron scale length. For the approach curve measurements, when the probe moved towards the passivated Zn, the degree of mediator diffusion obstruction increases, resulting in a gradual decrease in current, which is referred as negative feedback. Conversely, on the surface of the newly deposited Zn accelerate the feedback loop, the probe positioned closer to the substrate results in a gradual increase in current, which is referred as positive feedback. The corresponding kinetic parameters (k_f) were achieved by fitting the approach curve measurement results using analytical expressions from Cornut and Lefrou.[54, 55] The approach curve was collected at 0.4 V vs Ag/AgCl

with an approach rate of 20 μm s^{-1}. And the relationship between normalized current I_t/I_{inf} and normalized distance L = D/a has been reported in our previous work.[53]

SECM Feedback Imaging:

SECM is a powerful technique for mapping surface reactivity with high spatial and temporal resolution consisting of four-electrode systems with ultramicroelectrode (UME).[56] Feedback mode is the most commonly used SECM operating mode, where due to the feedback effect, the tip current depends on faradaic processes involving redox mediators (FcMeOH) in the electrolyte (aqueous $ZnSO_4$) to enable local tip-to-substrate electron transfer processes. When the SECM tip approaches the substrate, the species generated at the tip during the electrochemical process diffuse to the initial conductive Zn crystals surface, and generating a higher feedback current in comparison to the value far away from the substrate electrode, called positive feedback ($I_t/I_{inf} > 1$). Conversely, when the tip approached passivated Zn crystals, the tip current decreased, called negative feedback ($I_t/I_{inf} < 1$).[57]

Probe Approach Curves:

SECM approach curves can elucidate the localized electrochemical reaction activity and the rate-transferring stage of the interfacial process, we demonstrate a simple and reliable methodology for extraction of the rate constant (k) of a heterogeneous chemical reaction from steady-state SECM current-distance curves.[52, 58] In SECM with a conventional UME tip, the tip current can be recorded as a function of tip-to-substrate separation, d, as the tip approaches the substrate, and the normalized tip current can be employed to estimate absolute d.[59] These approach curves were obtained by the magnitude of the current with Pt UME of different distances (i.e., I_t vs L dependencies, where $I = I_{t(d)}/I_{inf}$ is the normalized tip current corresponding to a tip—substrate separation d, $i_{inf} = 4nFDc^*a$ is the tip current at an infinite tip—substrate distance; and L =d/a).[60] Equation 1 describes the SECM current—distance curve with finite heterogeneous kinetics at the substrate.[61, 62]

$$I_{inf} = \frac{I_t}{1+1/\Lambda c} + \frac{I'}{1+\Lambda c} \qquad (1)$$

where I_{inf} is the normalized tip current under kinetic control, I'= 0.68 + 0.3315 exp(-1.0672/L), Λc=kd/D (where k is the heterogeneous chemical or electrochemical rate constant and D is the diffusion coefficient), and the normalized diffusion control tip current is

$$I_t = \frac{0.78377}{L} + 0.3315\, e^{-1.0672/L} + 0.68 \qquad (2)$$

From eq 1, the expression for the maximum kinetically limited normalized tip current at d→ 0 is

$$I_{inf,max} = \lim_{d\to 0} I_{inf} = \pi ka/4D \qquad (3)$$

And the relative rate constant (k) analysis of the fitting formulation is from Cornut and Lefrou.[54, 63]

Probe Fabrication

Pt ultra-micro electrodes (UMEs) were prepared by sealing 10 μm Pt wire in a glass capillary (*o.d.*, 1.0 mm; *i.d.*, 0.58 mm; Sutter) under a gas oxygen flame. The pre-cleaned capillary should be moisture and dust free, refraining poor sealing of the glass around the Pt wire due to impurities and water. Afterward, the Pt tips were connected with wires through conductive silver epoxy. Next, the Pt probes were sharpened *via* grinding to decrease the area of glass around the Pt wire and reduce the total probe radius. After sharpening, the probes as SECM tips were polished until smooth. Finally, the geometry, size and smoothness of UMEs were observed with an optical microscope (Zeiss). And micrometer-sized SECM Pt tips have a radius of 5 μm with an RG of approximately 2.5 were fabricated via similar procedure listed in the above statement, as shown in Figure S28. As for nano-sized electrode preparation, Pt nanoelectrodes were prepared by pulling and heat sealing 5 μm radius Pt wires into borosilicate capillary glass (O.D., 1.0 mm; I.D., 0.2 mm) under vacuum with a HL-1000 pipet puller (Micrology (Wuhan) Precision Instruments, Ltd.). The produced nanoelectrodes were polished on 1 μm diamond polishing pads under video microscopic control. The electrodes were characterized by steady-state voltammetry, as shown in Figure S29.

Computational methods

To investigate the interfacial interaction between the deposited Zn (002) surface and the HOPG substrate, density functional theory (DFT) calculations were performed using the CP2K package with the Gaussian plane wave (GPW) method.[64] The Perdew-Burke-Ernzerhof (PBE)[65] exchange-

correlation functional was employed, along with the DFT-D3 correction with Becke-Johnson (BJ) damping[66, 67] to account for non-covalent interactions. Goedecker-Teter-Hutter (GTH) pseudopotentials[68] were used in combination with TZVP-MOLOPT basis sets.[69] The energy cutoff for the finest multigrid for plane waves was set to 400 Ry.

Moiré lattices were constructed using a single-layer graphene sheet and a single-layer Zn (002) surface. The experimental lattice constant of HOPG (2.46 Å) was used for the graphene sheet to represent the substrate used in the experiments, while the lattice constant of the 2D Zn plates (2.647 Å), as measured in this work, was used for the Zn layer. The Moiré lattice patterns were generated by constraining the lattice constant of the supercell to not exceed 20 times the lattice constant of the Zn unit cell and by rotating the layers until the lattice mismatch was smaller than 1%. A total of 32 rotation angles, ranging from 0° to 30°, were investigated. To compensate for the lattice mismatch, the graphene lattice constant was fixed at the experimental HOPG value, and the Zn layer distance was slightly adjusted (not more than 1%).

The interaction energy between the graphene sheet and the Zn layer was calculated by considering the energy difference between the combined system and the sum of the energies of the isolated components. The geometries were fixed during the calculations, but the distance between the graphene sheet and the Zn layer was sampled in a range around the van der Waals radius sum of carbon and zinc (3.09 Å) to estimate the optimal distance. The distances investigated were 3.09 Å, 3.11 Å, 3.13 Å, 3.17 Å, and 3.20 Å. For each rotation angle, a polynomial fit was used to estimate the optimal distance and the corresponding interaction energy at that distance.

Crystal number calculation methods

A total of 11 SEM images of the same Zn crystal deposited sample on HOPG with a capacity of 0.16 mA h cm^{-2} were selected for analysis. These images were used to calculate the number of crystals present in each plot. The computed distribution of the extent of crystals is detailed in Table S1. The rotation angle was calibrated by having one edge of a Zn crystal with a 0° rotation angle and adding auxiliary lines. The offset angles between the other crystal edge lines and the auxiliary line were calculated using the auxiliary line as a reference. The rotation angle of each crystal is also shown in the Table S1.

Cell assembling

All electrochemical properties were conducted by coin cells (CR2032), using glass fiber (GF) as separator. The diameters of Zn electrode, graphite paper and carbon paper are all 13 mm and the diameter of GF is 18 mm. The Zn|Graphite and Zn|Carbon asymmetric cells were fabricated with Zn foil as anode and graphite paper/carbon paper as cathode, with 150 μL, 1 M $ZnSO_4$ as the electrolyte to study the Zn plating/stripping behavior, nucleation process and CE. The cut-off voltage of Zn|Graphite and Zn|carbon cells was set to 0.5 V (vs. Zn/Zn^{2+}). All of the galvanostatic charge-discharge curves were assessed by a NEWARE battery testing system at various capacities at 30 °C.

ASSOCIATED CONTENT

Supporting Information. The Supporting Information is available free of charge on the ACS Publications website.

Chemicals and materials, probe fabrication and substrate fabrication and characterization, electrochemical measurements, SECM feedback imaging, probe approach fitting curves, optical images, X-ray photoelectron spectroscopy (XPS) survey and depth profiling curves, scanning electron microscopy (SEM) images, X-ray diffraction (XRD) patterns, High-resolution transmission electron microscope (HRTEM) images and energy dispersive X-ray spectroscopy (EDX), Atomic force microscope (AFM), Raman spectra, Feedback approaching curves on deposited Zn, SECM analysis of deposited Zn crystal with 5 μm and 500 nm probe, the chronoamperometry test curves, table of the ratio of summary of the specific distribution and rotation angle of each crystal in SEM images and crystal number calculation methods and cell assembling method (PDF).

AUTHOR INFORMATION

Corresponding Authors

* Jingshu Hui - College of Energy, Soochow Institute for Energy and Materials Innovations (SIEMIS), Key Laboratory of Advanced Carbon Materials and Wearable Energy Technologies of Jiangsu Province, Soochow University, Suzhou 215006, P.R. China

Email: jshui@suda.edu.cn

* Yang Yang – Theoretical Chemistry Institute and Department of Chemistry, University of Wisconsin-Madison, Madison, Wisconsin, United States
Email: yyang222@wisc.edu
* Zhongfan Liu - Center for Nanochemistry, Beijing Science and Engineering Center for Nanocarbons, Beijing National Laboratory for Molecular Sciences, College of Chemistry and Molecular Engineering, Peking University, Beijing, China**;** Technology Innovation Center of Graphene Metrology and Standardization for State Market Regulation, Beijing Graphene Institute, Beijing, China
Email: zfliu@pku.edu.cn

Authors

Jin Zhao - College of Energy, Soochow Institute for Energy and Materials InnovationS (SIEMIS), Key Laboratory of Advanced Carbon Materials and Wearable Energy Technologies of Jiangsu Province, Soochow University, Suzhou 215006, P.R. China
Zehua Chen - Theoretical Chemistry Institute and Department of Chemistry, University of Wisconsin-Madison, Madison, Wisconsin, United States
Zhihui Chen - College of Energy, Soochow Institute for Energy and Materials Innovations (SIEMIS), Key Laboratory of Advanced Carbon Materials and Wearable Energy Technologies of Jiangsu Province, Soochow University, Suzhou 215006, P.R. China
Zeyi Meng - College of Energy, Soochow Institute for Energy and Materials Innovations (SIEMIS), Key Laboratory of Advanced Carbon Materials and Wearable Energy Technologies of Jiangsu Province, Soochow University, Suzhou 215006, P.R. China
Jianwei Zhang - Institute of Functional Nano and Soft Materials (FUNSOM), Jiangsu Key Laboratory for Carbon-Based Functional Materials and Devices, Soochow University, Suzhou 215006, P.R. China
Wenjie Lv - College of Energy, Soochow Institute for Energy and Materials Innovations (SIEMIS), Key Laboratory of Advanced Carbon Materials and Wearable Energy Technologies of Jiangsu Province, Soochow University, Suzhou 215006, P.R. China
Congshan Guo - College of Energy, Soochow Institute for Energy and Materials Innovations (SIEMIS), Key Labora-tory of Advanced Carbon Materials and Wearable Energy Technologies of Jiangsu Province, Soochow University, Suzhou 215006, P.R. China

Zhizhen Lv - College of Energy, Soochow Institute for Energy and Materials Innovations (SIEMIS), Key Laboratory of Advanced Carbon Materials and Wearable Energy Technologies of Jiangsu Province, Soochow University, Suzhou 215006, P.R. China
Shouce Huang - College of Energy, Soochow Institute for Energy and Materials Innovations (SIEMIS), Key Laboratory of Advanced Carbon Materials and Wearable Energy Technologies of Jiangsu Province, Soochow University, Suzhou 215006, P.R. China

Author contributions

J.Z. and J.H. conceived the idea and wrote the manuscript. J.Z. carried out experiments and measurements. Z.C and Y.Y designed theoretical modeling and completed relevant theoretical calculations data analysis. J.Z. and Z.C. performed AFM experiments and schematic diagrams. J.Z. and Z.M. carried out XRD characterization and participated in discussions. J.Z. and Z.L. characterized SEM images. J.Z. performed TEM experiments. C.G. provided the SECM nano tips. S.H. accomplished Zn crystal number statistics. Y.Y. supervised the simulations and calculations, J.Z. and J.L. conducted electrochemical performance test, Z.L. and J.H. supervised the study and the manuscript writing. All authors discussed the results.

Notes

The authors declare no competing financial interest.

ACKNOWLEDGMENT

This work is supported by the National Natural Science Foundation of China (Grant No. 22204115), Natural Science Foundation of Jiangsu Province (Grant No. BK20220485), Suzhou Municipal Science and Technology Bureau (Grant No. ZXL2022494), National Science Foundation (Grant no. 2238473) from the University of Wisconsin via the Wisconsin Alumni Research Foundation, and start-up research grant for a distinguished professor at Soochow University (J.H.).

REFERENCES

1. Zheng, J. X.; Kim, M. S.; Tu, Z. Y.; Choudhury, S.; Tang, T.; Archer, L. A., Regulating Electrodeposition Morphology of Lithium: towards Commercially Relevant Secondary Li Metal Batteries. *Chem. Soc. Rev.* **2020,** *49* (9), 2701-2750.

2. Biswal, P.; Kludze, A.; Rodrigues, J.; Deng, Y.; Moon, T.; Stalin, S.; Zhao, Q.; Yin, J. F.; Kourkoutis, L. F.; Archer, L. A., The Early-stage Growth and Reversibility of Li Electrodeposition in Br-rich Electrolytes. *Proc. Natl. Acad. Sci.* **2021,** *118* (2), e201207118.
3. Zheng, J. X.; Zhao, Q.; Tang, T.; Yin, J. F.; Quilty, C. D.; Renderos, G. D.; Liu, X. T.; Deng, Y.; Wang, L.; Bock, D. C.; Jaye, C.; Zhang, D. H.; Takeuchi, E. S.; Takeuchi, K. J.; Marschilok, A. C.; Archer, L. A., Reversible Epitaxial Electrodeposition of Metals in Battery Anodes. *Science* **2019,** *366* (6465), 645-648.
4. Zhao, Z. D.; Wang, R.; Peng, C. X.; Chen, W. J.; Wu, T. Q.; Hu, B.; Weng, W. J.; Yao, Y.; Zeng, J. X.; Chen, Z. H.; Liu, P. Y.; Liu, Y. C.; Li, G. S.; Guo, J.; Lu, H. B.; Guo, Z. P., Horizontally Arranged Zinc Platelet Electrodeposits Modulated by Fluorinated Covalent Organic Framework Film for High-rate and Durable Aqueous Zinc Ion Batteries. *Nat. Commun.* **2021,** *12* (1), 6606.
5. Zheng, X. H.; Liu, Z. C.; Sun, J. F.; Luo, R. H.; Xu, K.; Si, M. Y.; Kang, J.; Yuan, Y.; Liu, S.; Ahmad, T.; Jiang, T. L.; Chen, N.; Wang, M. M.; Xu, Y.; Chuai, M.; Zhu, Z. X.; Peng, Q.; Meng, Y. H.; Zhang, K.; Wang, W. P.; Chen, W., Constructing Robust Heterostructured Interface for Anode-free Zinc Batteries with Ultrahigh Capacities. *Nat. Commun.* **2023,** *14* (1), 76.
6. Zhao, Z. X.; He, Y.; Yu, W. T.; Shang, W. X.; Ma, Y. Y.; Tan, P., Revealing the Missing Puzzle Piece of Concentration in Regulating Zn Electrodeposition. *Proc. Natl. Acad. Sci.* **2023,** *120* (44), e2307847120.
7. Zheng, J. C.; Yin, J. F.; Zhang, D. H.; Li, G. J.; Bock, D. C.; Tang, T.; Zhao, Q.; Liu, X. T.; Warren, A.; Deng, Y.; Jin, S.; Marschilok, A.; Takeuchi, E. S.; Takeuchi, K. J.; Rahn, C. D.; Archer, L. A., Spontaneous and Field-induced Crystallographic Reorientation of Metal Electrodeposits at Battery Anodes. *Sci. Adv.* **2020,** *6* (25), eabb1122
8. Zhang, W. D.; Zhao, Q.; Hou, Y. P.; Shen, Z. Y.; Fan, L.; Zhou, S. D.; Lu, Y. Y.; Archer, L. A., Dynamic Interphase-mediated Assembly for Deep Cycling Metal Batteries. *Sci. Adv.* **2021,** *7* (49), eabl3752.
9. Cai, Z.; Wang, J.; Sun, Y., Anode corrosion in aqueous Zn metal batteries. *eScience* **2023,** *3* (1), 100093.
10. Zheng, J. X.; Archer, L. A., Controlling Electrochemical Growth of Metallic Zinc Electrodes: Toward Affordable Rechargeable Energy Storage Systems. *Sci. Adv.* **2021,** *7* (2), eabe0219.
11. Wu, J.; Yuan, C. G.; Li, T. Y.; Yuan, Z. Z.; Zhang, H. M.; Li, X. F., Dendrite-Free Zinc-Based Battery with High Areal Capacity via the Region-Induced Deposition Effect of Turing Membrane. *J. Am. Chem. Soc.* **2021,** *143* (33), 13135-13144.
12. Yang, Q.; Bang, G. J.; Guo, Y.; Liu, Z. X.; Yon, B. X.; Wang, D. H.; Huang, Z. D.; Li, X. L.; Fan, J.; Zhi, C. Y., Do Zinc Dendrites Exist in Neutral Zinc Batteries: A Developed Electrohealing Strategy to In Situ Rescue In-Service Batteries. *Adv. Mater.* **2019,** *31* (43), 1903778.
13. Yu, X. Y.; Li, Z. G.; Wu, X. H.; Zhang, H. T.; Zhao, Q. G.; Liang, H. F.; Wang, H.; Chao, D. L.; Wang, F.; Qiao, Y.; Zhou, H. S.; Sun, S. G., Perspective Ten Concerns of Zn Metal Anode for Rechargeable Aqueous Zinc Batteries. *Joule* **2023,** *7* (6), 1145-1175.
14. Zhang, Q.; Luan, J. Y.; Huang, X. B.; Wang, Q.; Sun, D.; Tang, Y. G.; Ji, X. B.; Wang, H. Y., Revealing the Role of Crystal Orientation of Protective Layers for Stable Zinc Anode. *Nat. Commun.* **2020,** *11* (1), 3961.

15. Zhang, Q.; Ma, Y. L.; Lu, Y.; Ni, Y. X.; Lin, L.; Hao, Z. K.; Yan, Z. H.; Zhao, Q.; Chen, J., Halogenated Zn Solvation Structure for Reversible Zn Metal Batteries. *J. Am. Chem. Soc.* **2022,** *144* (40), 18435-18443.
16. Jia, X. X.; Liu, C. F.; Neale, Z. G.; Yang, J. H.; Cao, G. Z., Active Materials for Aqueous Zinc Ion Batteries: Synthesis, Crystal Structure, Morphology, and Electrochemistry. *Chem. Rev.* **2020,** *120* (15), 7795-7866.
17. Zhao, Y. X.; Guo, S.; Chen, M. J.; Lu, B. A.; Zhang, X. T.; Liang, S. Q.; Zhou, J., Tailoring Grain Boundary Stability of Zinc-titanium Alloy for Long-lasting Aqueous Zinc Batteries. *Nat. Commun.* **2023,** *14* (1), 7080.
18. Wang, T.; Sun, J. M.; Hua, Y. B.; Krishna, B. N. V.; Xi, Q.; Ai, W.; Yu, J. S., Planar and Dendrite-free Zinc Deposition Enabled by Exposed Crystal Plane Optimization of Zinc Anode. *Energy Stor. Mater.* **2022,** *53*, 273-304.
19. Häussermann, U.; Simak, S. I., Origin of the c/a Variation in Hexagonal Close-packed Divalent Metals. *Phys. Rev. B* **2001,** *64* (24), 25114.
20. Yang, Q.; Li, Q.; Liu, Z.; Wang, D.; Guo, Y.; Li, X.; Tang, Y.; Li, H.; Dong, B.; Zhi, C., Dendrites in Zn‐Based Batteries. *Adv. Mater.* **2020,** *32* (48), 2001854.
21. Yang, F. H.; Yuwono, J. A.; Hao, J. N.; Long, J.; Yuan, L. B.; Wang, Y. Y.; Liu, S. L.; Fan, Y. M.; Zhao, S. Y.; Davey, K.; Guo, Z. P., Understanding H_2 Evolution Electrochemistry to Minimize Solvated Water Impact on Zinc-Anode Performance. *Adv. Mater.* **2022,** *34* (45), 2206754.
22. Yuan, L.; Hao, J.; Johannessen, B.; Ye, C.; Yang, F.; Wu, C.; Dou, S.-X.; Liu, H.-K.; Qiao, S.-Z., Hybrid working mechanism enables highly reversible Zn electrodes. *eScience* **2023,** *3* (2), 100096.
23. Zheng, J. X. K.; Yin, J. F.; Tang, T.; Archer, L. A., Moss-like Growth of Metal Electrodes: On the Role of Competing Faradaic Reactions and Fast Charging. *ACS Energy Lett.* **2023,** *8* (5), 2113-2121.
24. Hao, Z.; Zhang, Y.; Hao, Z.; Li, G.; Lu, Y.; Jin, S.; Yang, G.; Zhang, S.; Yan, Z.; Zhao, Q.; Chen, J., Metal Anodes with Ultrahigh Reversibility Enabled by the Closest Packing Crystallography for Sustainable Batteries. *Adv. Mater.* **2023,** *35* (9), 2209985.
25. Liu, H. Y.; Ye, Q.; Lei, D.; Hou, Z. D.; Hua, W.; Yu, H. Y.; Li, N.; Wei, C. G.; Kang, F. Y.; Wang, J. G., Molecular Brush: An Ion-redistributor to Homogenize Fast Zn Flux and Deposition for Calendar-life Zn Batteries. *Energy Environ. Sci.* **2023,** *16* (4), 1610-1619.
26. Yang, Q.; Li, L.; Hussain, T.; Wang, D.; Hui, L.; Guo, Y.; Liang, G.; Li, X.; Chen, Z.; Huang, Z.; Li, Y.; Xue, Y.; Zuo, Z.; Qiu, J.; Li, Y.; Zhi, C., Stabilizing Interface pH by N‐Modified Graphdiyne for Dendrite-Free and High-Rate Aqueous Zn-Ion Batteries. *Angew. Chem. Int. Ed.* **2021,** *61* (6), e202112304
27. Yang, Z. F.; Hu, C.; Zhang, Q.; Wu, T. Q.; Xie, C. L.; Wang, H.; Tang, Y. G.; Ji, X. B.; Wang, H. Y., Bulk-Phase Reconstruction Enables Robust Zinc Metal Anodes for Aqueous Zinc-Ion Batteries. *Angew. Chem. Int. Ed.* **2023,** *62* (35), e202308017.
28. Xie, C. L.; Liu, S. F.; Zhang, W. X.; Ji, H. M.; Chu, S. Q.; Zhang, Q.; Tang, Y. G.; Wang, H. Y., Robust and Wide Temperature-Range Zinc Metal Batteries with Unique Electrolyte and Substrate Design. *Angew. Chem. Int. Ed.* **2023,** *62* (28), e202304259.
29. Peng, M. K.; Tang, X. N.; Xiao, K.; Hu, T.; Yuan, K.; Chen, Y. W., Polycation-Regulated Electrolyte and Interfacial Electric Fields for Stable Zinc Metal Batteries. *Angew. Chem. Int. Ed.* **2023,** *62* (27), e202302701.

30. Li, G. J.; Zhao, Z. H.; Zhang, S. L.; Sun, L.; Li, M. N.; Yuwono, J. A.; Mao, J. F.; Hao, J. N.; Vongsvivut, J.; Xing, L. D.; Zhao, C. X.; Guo, Z. P., A Biocompatible Electrolyte Enables Highly Reversible Zn Anode for Zinc Ion Battery. *Nat. Commun.* **2023,** *14* (1), 6526.
31. Zhang, Y.; Zhang, Y. X.; Deng, J.; Xue, R. R.; Yang, S. C.; Ma, Y.; Wang, Z. H., In Situ Electrochemically-Bonded Self-Adapting Polymeric Interface for Durable Aqueous Zinc Ion Batteries. *Adv. Funct. Mater.* **2024,** *34* (6), 2310995.
32. Liu, M.; Yuan, W.; Ma, G.; Qiu, K.; Nie, X.; Liu, Y.; Shen, S.; Zhang, N., In‐Situ Integration of a Hydrophobic and Fast-Zn^{2+}-Conductive Inorganic Interphase to Stabilize Zn Metal Anodes. *Angew. Chem. Int. Ed.* **2023,** *62* (27), e202304444.
33. Youssef, K. M.; Koch, C. C.; Fedkiw, P. S., Influence of Pulse Plating Parameters on the Synthesis and Preferred Orientation of Nanocrystalline Zinc from Zinc Sulfate Electrolytes. *Electrochim. Acta* **2008,** *54* (2), 677-683.
34. Wu, S.; Hu, Z.; He, P.; Ren, L.; Huang, J.; Luo, J., Crystallographic engineering of Zn anodes for aqueous batteries. *eScience* **2023,** *3* (3), 100120.
35. Zhang, H. W.; Zhong, Y.; Li, J. B.; Liao, Y. Q.; Zeng, J. L.; Shen, Y.; Yuan, L. X.; Li, Z.; Huang, Y. H., Inducing the Preferential Growth of Zn (002) Plane for Long Cycle Aqueous Zn-Ion Batteries. *Adv. Energy Mater.* **2023,** *13* (1), 2203254.
36. Zhou, M.; Guo, S.; Li, J. L.; Luo, X. B.; Liu, Z. X.; Zhang, T. S.; Cao, X. X.; Long, M. Q.; Lu, B. G.; Pan, A. Q.; Fang, G. Z.; Zhou, J.; Liang, S. Q., Surface-Preferred Crystal Plane for a Stable and Reversible Zinc Anode. *Adv. Mater.* **2021,** *33* (21), 2100187.
37. Ren, L. X.; Hu, Z. L.; Peng, C. X.; Zhang, L.; Wang, N.; Wang, F.; Xia, Y. Y.; Zhang, S. J.; Hu, E. Y.; Luo, J. Y., Suppressing Metal Corrosion through Identification of Optimal Crystallographic Plane for Zn Batteries. *Proc. Natl. Acad. Sci.* **2024,** *121* (5), e2309981121.
38. Yi, Z.; Chen, G.; Hou, F.; Wang, L.; Liang, J., Strategies for the Stabilization of Zn Metal Anodes for Zn‐Ion Batteries. *Adv. Energy Mater.* **2020,** *11* (1), 2003065.
39. Zheng, J.; Deng, Y.; Yin, J.; Tang, T.; Garcia-Mendez, R.; Zhao, Q.; Archer, L. A., Textured Electrodes: Manipulating Built‐In Crystallographic Heterogeneity of Metal Electrodes via Severe Plastic Deformation. *Adv. Mater.* **2021,** *34* (1), 2106867.
40. Zheng, J. X.; Archer, L. A., Crystallographically Textured Electrodes for Rechargeable Batteries: Symmetry, Fabrication, and Characterization. *Chem. Rev.* **2022,** *122* (18), 14440-14470.
41. Yufit, V.; Tariq, F.; Eastwood, D. S.; Biton, M.; Wu, B.; Lee, P. D.; Brandon, N. P., Operando Visualization and Multi-scale Tomography Studies of Dendrite Formation and Dissolution in Zinc Batteries. *Joule* **2019,** *3* (2), 485-502.
42. Xie, C. L.; Liu, S. F.; Yang, Z. F.; Ji, H. M.; Zhou, S. H.; Wu, H.; Hu, C.; Tang, Y. G.; Ji, X. B.; Zhang, Q.; Wang, H. Y., Discovering the Intrinsic Causes of Dendrite Formation in Zinc Metal Anodes: Lattice Defects and Residual Stress. *Angew. Chem. Int. Ed.* **2023,** *62* (16), e202218612.
43. Eaglesham, D.; Gossmann, H. J.; Cerullo, M., Limiting Thickness h_{epi} for Epitaxial Growth and Room-temperature Si Growth on Si(100). *Phys. Rev. Lett.* **1990,** *65* (10), 1227-1230.
44. Yuan, Y.; Pu, S. D.; Pérez-Osorio, M. A.; Li, Z. X.; Zhang, S. M.; Yang, S. X.; Liu, B. Y.; Gong, C.; Menon, A. S.; Piper, L. F. J.; Gao, X. W.; Bruce, P. G.; Robertson, A. W., Diagnosing the Electrostatic Shielding Mechanism for Dendrite Suppression in Aqueous Zinc Batteries. *Adv. Mater.* **2023,** *36* (9), 2307708.
45. Mu, Y. B.; Li, Z.; Wu, B. K.; Huang, H. D.; Wu, F. H.; Chu, Y. Q.; Zou, L. F.; Yang, M.; He, J. F.; Ye, L.; Han, M. S.; Zhao, T. S.; Zeng, L., 3D Hierarchical Graphene Matrices Enable Stable Zn Anodes for Aqueous Zn Batteries. *Nat. Commun.* **2023,** *14* (1), 4205.

46. Zhou, J. H.; Xie, M.; Wu, F.; Mei, Y.; Hao, Y. T.; Huang, R. L.; Wei, G. L.; Liu, A. N.; Li, L.; Chen, R. J., Ultrathin Surface Coating of Nitrogen-Doped Graphene Enables Stable Zinc Anodes for Aqueous Zinc-Ion Batteries. *Adv. Mater.* **2021,** *33* (33), 2101649.
47. Zandiatashbar, A.; Lee, G.-H.; An, S. J.; Lee, S.; Mathew, N.; Terrones, M.; Hayashi, T.; Picu, C. R.; Hone, J.; Koratkar, N., Effect of defects on the intrinsic strength and stiffness of graphene. *Nat. Commun.* **2014,** *5* (1), 3186.
48. Ilchenko, O.; Pilgun, Y.; Kutsyk, A.; Bachmann, F.; Slipets, R.; Todeschini, M.; Okeyo, P. O.; Poulsen, H. F.; Boisen, A., Fast and quantitative 2D and 3D orientation mapping using Raman microscopy. *Nat. Commun.* **2019,** *10* (1), 5555.
49. Du, W. C.; Ang, E. H. X.; Yang, Y.; Zhang, Y. F.; Ye, M. H.; Li, C. C., Challenges in the Material and Structural Design of Zinc Anode towards High-performance Aqueous Zinc-ion Batteries. *Energy Environ. Sci.* **2020,** *13* (10), 3330-3360.
50. Du, W. C.; Yan, J. P.; Cao, C. H.; Li, C. C., Electrocrystallization Orientation Regulation of Zinc Metal Anodes: Strategies and Challenges. *Energy Stor. Mater.* **2022,** *52*, 329-354.
51. Zheng, Z. Y.; Zhong, X. W.; Zhang, Q.; Zhang, M. T.; Dai, L. X.; Xiao, X.; Xu, J. H.; Jiao, M. L.; Wang, B. R.; Li, H.; Jia, Y. Y.; Mao, R.; Zhou, G. M., An Extended Substrate Screening Strategy Enabling a Low Lattice Mismatch for Highly Reversible Zinc Anodes. *Nat. Commun.* **2024,** *15* (1), 753.
52. Hui, J. S.; Gossage, Z. T.; Sarbapalli, D.; Hernández-Burgos, K.; Rodríguez-López, J., Advanced Electrochemical Analysis for Energy Storage Interfaces. *Anal. Chem.* **2019,** *91* (1), 60-83.
53. Zhao, J.; Lv, Z. Z.; Wang, S. J.; Chen, Z. H.; Meng, Z. Y.; Li, G. X.; Guo, C. S.; Liu, T. T.; Hui, J. S., Interphase Modulated Early-Stage Zn Electrodeposition Mechanism. *Small Methods* **2023,** *7* (11), 2300731.
54. Lefrou, C.; Cornut, R., Analytical Expressions for Quantitative Scanning Electrochemical Microscopy (SECM). *Chemphyschem* **2010,** *11* (3), 547-556.
55. Wang, Q. A.; Rodríguez-López, J.; Bard, A. J., Evaluation of the Chemical Reactions from Two Electrogenerated Species in Picoliter Volumes by Scanning Electrochemical Microscopy. *Chemphyschem* **2010,** *11* (13), 2969-2978.
56. Kwak, J.; Bard, A. J., Scanning Electrochemical Microscopy. Apparatus and Two-Dimensional Scans of Conductive and Insulating Substrates. *Anal. Chem.* **1989,** *61*, 1794-1799.
57. Patrick R. Unwin; Bard, A. J., Scanning Electrochemical Microscopy. 9. Theory and Application of the Feedback Mode to the Measurement of Following Chemical Reaction Rates in Electrode Processes. *J. Phys. Chem.* **1991,** *95*, 7814-7824.
58. Wipf, D. O.; Bard, A. J., Scanning Electrochemical Microscopy.X. High Resolution Imaging of Active Sites on an Electrode Surface. *J. Electrochern. Soc.* **1991,** *138*, L4-L6.
59. Chang Wei; Bard, A. J., Scanning Electrochemical Microscopy. 28. Ion-Selective Neutral Carrier-Based Microelectrode Potentiometry. *Anal. Chem.* **1995,** *67*, 1346-1356.
60. Treichel, D. A.; Mirkin, M. V.; Bard, A. J., Scanning Electrochemical Microscopy. 27. Application of a Simplified Treatment of an Irreversible Homogeneous Reaction following Electron Transfer to the Oxidative Dimerization of 4-Nitrophenolate in Acetonitrile. *J. Phys. Chem.* **1994,** *98*, 5751-5757.
61. Meral Arca; Michael V. Mirkin; Bard, A. J., Polymer Films on Electrodes. 26. Study of Ion Transport and Electron Transfer at Polypyrrole Films by Scanning Electrochemical Microscopy. *J. Phys. Chem.* **1995,** *99*, 5040-5050.

62. Mirkin, M. V.; Area, M.; Bard, A. J., Scanning Electrochemical Microscopy. 22. Examination of Thin Solid Films of AgBr: Ion Diffusion in the Film and Heterogeneous Kinetics at the Film/Solution Interface. *J. Phys. Chem.* **1993,** *97*, 10790-10795.
63. Cornut, R.; Bhasin, A.; Lhenry, S.; Etienne, M.; Lefrou, C., Accurate and simplified consideration of the probe geometrical defaults in scanning electrochemical microscopy: theoretical and experimental investigations. *Anal. Chem.* **2011,** *83* (24), 9669-75.
64. Lippert, B. G.; Parrinello, J. H.; Michele, A hybrid Gaussian and plane wave density functional scheme. *Mol. Phys.* **1997,** *92* (3), 477-488.
65. John P. Perdew, K. B., Matthias Ernzerhof, Generalized Gradient Approximation Made Simple. *Phys. Rev. Lett.* **1996,** *77* (18), 3865-3868.
66. Grimme, S.; Antony, J.; Ehrlich, S.; Krieg, H., A consistent and accurate ab initio parametrization of density functional dispersion correction (DFT-D) for the 94 elements H-Pu. *J. Chem. Phys.* **2010,** *132* (15), 154104.
67. Grimme, S.; Ehrlich, S.; Goerigk, L., Effect of the damping function in dispersion corrected density functional theory. *J. Comput. Chem.* **2011,** *32* (7), 1456-1465.
68. Goedecker, S.; Teter, M.; Hutter, J., Separable dual-space Gaussian pseudopotentials. *Phys. Rev. B* **1996,** *54* (3), 1703-1710.
69. VandeVondele, J.; Hutter, J., Gaussian basis sets for accurate calculations on molecular systems in gas and condensed phases. *J. Chem. Phys.* **2007,** *127* (11), 114105.

Table of Contents